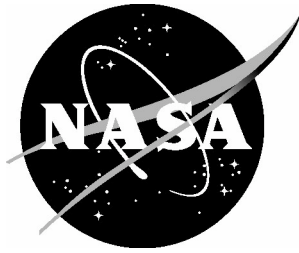# Buckling and Failure of Compression-Loaded Composite Cylindrical Shells With Geometric and Material Imperfections

Mark W. Hilburger and James H. Starnes, Jr.
Langley Research Center, Hampton, Virginia

Since its founding, NASA has been dedicated to the advancement of aeronautics and space science. The NASA Scientific and Technical Information (STI) Program Office plays a key part in helping NASA maintain this important role.

The NASA STI Program Office is operated by Langley Research Center, the lead center for NASA's scientific and technical information. The NASA STI Program Office provides access to the NASA STI Database, the largest collection of aeronautical and space science STI in the world. The Program Office is also NASA's institutional mechanism for disseminating the results of its research and development activities. These results are published by NASA in the NASA STI Report Series, which includes the following report types:
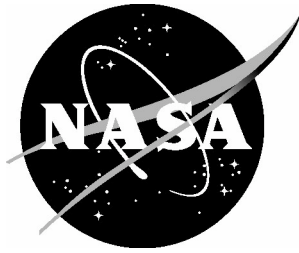
- TECHNICAL PUBLICATION. Reports of completed research or a major significant phase of research that present the results of NASA programs and include extensive data or theoretical analysis. Includes compilations of significant scientific and technical data and information deemed to be of continuing reference value. NASA counterpart of peer-reviewed formal professional papers, but having less stringent limitations on manuscript length and extent of graphic presentations.

- TECHNICAL MEMORANDUM. Scientific and technical findings that are preliminary or of specialized interest, e.g., quick release reports, working papers, and bibliographies that contain minimal annotation. Does not contain extensive analysis.

- CONTRACTOR REPORT. Scientific and technical findings by NASA-sponsored contractors and grantees.

- CONFERENCE PUBLICATION. Collected papers from scientific and technical conferences, symposia, seminars, or other meetings sponsored or co-sponsored by NASA.

- SPECIAL PUBLICATION. Scientific, technical, or historical information from NASA programs, projects, and missions, often concerned with subjects having substantial public interest.

- TECHNICAL TRANSLATION. English-language translations of foreign scientific and technical material pertinent to NASA's mission.

Specialized services that complement the STI Program Office's diverse offerings include creating custom thesauri, building customized databases, organizing and publishing research results ... even providing videos.

For more information about the NASA STI Program Office, see the following:

- Access the NASA STI Program Home Page at *http://www.sti.nasa.gov*

- E-mail your question via the Internet to help@sti.nasa.gov

- Fax your question to the NASA STI Help Desk at (301) 621-0134

- Phone the NASA STI Help Desk at (301) 621-0390

- Write to:
  NASA STI Help Desk
  NASA Center for AeroSpace Information
  7121 Standard Drive
  Hanover, MD 21076-1320

Buckling and Failure of Compression-Loaded Composite Cylindrical Shells With Geometric and Material Imperfections

Mark W. Hilburger and James H. Starnes, Jr.
Langley Research Center, Hampton, Virginia

September 2004

Available from:

Abstract

The results of an experimental and numerical study of the effects of initial imperfections on the buckling response and failure of unstiffened thin-walled compression-loaded graphite-epoxy cylindrical shells are presented. The shells considered in the study have six different orthotropic or quasi-isotropic shell-wall laminates and two different shell-radius-to-thickness ratios. The numerical results include the effects of geometric shell-wall mid-surface imperfections, shell-wall thickness variations, local shell-wall ply-gaps associated with the fabrication process, shell-end geometric imperfections, nonuniform end loads, and the effects of elastic boundary conditions. Selected cylinder parameter uncertainties were also considered. Results that illustrate the effects of imperfections and uncertainties on the nonlinear response characteristics, buckling loads and failure of the shells are presented. In addition, a common failure analysis is used to predict material failures in the shells.

Introduction

The increasing need to produce lighter-weight aerospace shell structures has led to the use of advanced material systems in new structural designs, and improved design methods appropriate for these advanced material systems are needed. The high strength-to-weight and high stiffness-to-weight ratios of advanced composite materials offer significant weight reduction potential for aerospace structures. In addition, the use of advanced composite materials allows the designer to tailor the stiffness properties of composite structures to obtain structurally efficient designs. Designers often use a design-level analysis procedure with empirical data to develop new structural designs for strength and buckling critical structures. The traditional approach for designing thin-walled buckling-resistant isotropic shell structures is to predict the buckling load of the shell with a deterministic analysis, and then to reduce this predicted load with an empirical "knockdown" factor (e.g., Ref. 1). The empirical knockdown factor is intended to account for the difference between the predicted buckling load and the actual buckling load for the shell determined from tests. A linear bifurcation buckling analysis is often used for the design-level analysis, and this analysis is usually based on nominal structural dimensions and material properties of an idealized, geometrically perfect shell. The design knockdown factor used in the design of buckling-resistant shells is often based on the "lower bound" design recommendations reported in Reference 1. This design philosophy can result in overly conservative designs for these structures, and it can potentially even result in unconservative designs if the empirical data are not representative of the design of interest. While it is generally recognized that initial geometric shell-wall imperfections are a major contributor to the discrepancy between the predicted shell buckling loads and the experimentally measured shell buckling loads (e.g., Refs. 2-6), the traditional sources of design knockdown factors do not include data or information for shell structures made from advanced composite materials. In addition, the traditional sources of design knockdown factors for predicting shell buckling loads do not include information related to the sensitivity of the response of a shell to various forms of imperfections. Recent studies (e.g., Refs. 7-12) have shown that traditional initial geometric shell-wall imperfections, and other nontraditional forms of imperfections or variations in geometric and material parameters, fabrication related anomalies, loading conditions, and boundary conditions can significantly affect the buckling load of a compression-loaded composite shell structure. The effects of these traditional and nontraditional classes of initial imperfections on the buckling of composite shells are generally not well understood by structural engineers and designers. It has been shown by Hilburger and Starnes (e.g., Refs. 11 and 12) that highly

accurate predictions of the nonlinear response and buckling load of a compression-loaded shell can be obtained when the initial geometric imperfections, material properties, shell-wall thickness distribution, and other features are modeled to a high degree of accuracy. Modern high-fidelity nonlinear analysis procedures offer the opportunity to improve some of the engineering approximations that are used in the design and analysis of shell structures, and to provide insight into the effects of traditional and nontraditional imperfections on the response of compression-loaded composite shell structures.

The present paper describes the results of an experimental and analytical study of selected unstiffened thin-walled compression-loaded graphite-epoxy cylindrical shell. The analytical results include the effects of traditional initial geometric shell-wall imperfections, and the effects of nontraditional initial imperfections and uncertainties in other geometric and material parameters, loading conditions, and boundary conditions. The results of six graphite-epoxy shells with different shell-wall laminates are presented. The shell-wall laminates include four orthotropic laminates and two quasi-isotropic laminates. The two orthotropic shells and one of the quasi-isotropic shell have shell-radius-to-thickness ratios equal to 200, and two orthotropic shells the other quasi-isotropic shell have shell-radius-to-thickness ratios equal to 100. The response of three shells with shell-radius-to-thickness ratios equal to 100 are presented as examples of a thin-walled shells that exhibit material failures before or during buckling, and the material failures cause the overall failure of the shell and no postbuckling load carrying capacity. The response of three shells with shell-radius-to-thickness ratios equal to 200 are presented as contrasting examples of thin-walled shells that exhibit significant postbuckling load carrying capacity and material failures occur in the postbuckling range of loading. A common material failure analyses is used to predict material failures in the shell. Traditional shell-wall geometric imperfections and several nontraditional imperfections were measured, and representations of these imperfections have been included in nonlinear analyses of the shells. In addition, selected uncertainties in several geometric, material, and loading parameters were characterized and were also included in the analyses. The effects of initial geometric shell-wall imperfections, shell-wall thickness variations, shell-end geometric imperfections, nonuniform applied end loads, and variations in the boundary conditions, including the effects of elastic boundary conditions, on the buckling response of these thin-walled composite shells are discussed in the present paper. The nonlinear analyses were conducted with the geometrically nonlinear STAGS finite element analysis code (Ref. 13). The results of the study are used to illustrate the significance of initial imperfections and uncertainties on composite shell response characteristics. The nonlinear shell analysis procedure used to predict the nonlinear response and buckling loads of the shells is described, and the analysis results are compared with the experimental results. The use of this nonlinear shell analysis procedure for determining accurate, high-fidelity design knockdown factors for shell buckling, collapse, and failure, and for determining the effects of variations and uncertainties in shell geometric and material parameters on shell response is discussed.

Test Specimens, Imperfection Measurements, and Test Apparatus and Tests

Test Specimens

The specimens tested in this investigation were fabricated from 12-in-wide, 0.005-in.-thick AS4/3502 graphite-epoxy preimpregnated unidirectional tape material made by Hercules, Inc. The nominal unidirectional lamina properties of a typical 0.005-in.-thick ply with a fiber volume fraction of 0.62 are as follows: longitudinal compression modulus E_1 = 18.5 Msi, transverse modulus E_2 = 1.64 Msi, in-plane shear modulus G_{12} = 0.87 Msi, and major Poisson's ratio ν_{12} = 0.30.   The material was laid up on a 15.75-in.-diameter mandrel and cured in an autoclave to form six shells with different shell-wall laminates and include an 8-ply axially stiff $[\mp45/0_2]_s$ laminate, an 8-ply circumferentially stiff $[\mp45/90_2]_s$ laminate, an 8-ply quasi-isotropic $[\mp45/0/90]_s$ laminate, a 16-ply axially stiff $[\mp45/0_2]_{2s}$ laminate, a 16-

ply circumferentially stiff $[\mp45/90_2]_{2s}$ laminate, and a 16-ply quasi-isotropic $[\mp45/0/90]_{2s}$ laminate. The resulting six shells are referred to herein as shells or specimens C1 through C6, respectively. These specimens had a nominal length of 16.0 in. and a nominal radius of 8.0 in. The 8-ply and 16-ply specimens had a nominal shell-wall thickness of 0.04 in. and 0.08 in., respectively. Both ends of the specimens were potted in an aluminum-filled epoxy resin to assure that the ends of the specimens did not fail prematurely during the test. The potting material extended approximately 1.0 inch along the length of the specimens at each end resulting in a test section that was approximately 14.0 in. long. The ends of the specimens were machined flat and parallel to facilitate proper load introduction during the tests. A photograph of a typical specimen and the specimen coordinate system used to represent the corresponding geometry is shown in Fig.1. The shell length, test-section length, radius, and thickness are designated as L, L_T, R and t, respectively.

Imperfection Measurements

Three-dimensional surveys of the inner and outer shell-wall surfaces of the specimens were made prior to testing the specimens to determine their initial geometric shell-wall imperfection shapes and shell-wall thickness distributions. Measurements were taken over a uniform grid with increments of 0.125 in. in the axial direction and 0.139 in. (approximately 1° of arc) in the circumferential direction over the exposed surfaces of the specimens. The inner surface measurement was used to determine the initial geometric shell-wall imperfection shape of a specimen, and the difference between the outer and inner surface measurements was used to determine the shell-wall thickness distribution. A contour plot of the nondimensionalized initial geometric shell-wall mid-surface imperfections $\overline{w}_o(x,\theta)$ for specimen C3 is shown in Fig. 2. The measured shell-wall imperfection w_o is normalized by the average measured shell-wall thickness $t_{ave} = 0.0381$ inches. These results indicate that the initial geometric shell-wall imperfection is periodic in the circumferential direction and exhibits slight variations in the axial direction. The amplitude of the imperfection varies from $+1.341 t_{ave}$ to $-1.535\ t_{ave}$. A contour plot of the nondimensionalized shell-wall thickness variation $\overline{t}_o(x,\theta)$ for specimen C3 is shown in Fig. 3, where the measured thickness value t_o is normalized by the average measured shell-wall thickness t_{ave}. These results indicate that the shell-wall thickness, and hence the laminate stiffnesses, varies significantly over a short distance. The thickness varies from 0.928 to 1.321 times t_{ave}. Most of the thickness variation is attributed to local variations in the resin content of the laminate associated with the fabrication process. However, the dark-blue angular pattern in the thickness distribution is attributed to small gaps between adjacent pieces of graphite-epoxy tape in some of the laminate plies that were generated during the lay-up and curing processes. Such a region is referred to herein as a lamina ply-gap or a ply-gap. These locally thin shell-wall regions have a significant shell-wall mid-surface eccentricity, and have reduced stiffnesses relative to the rest of the shell wall. Lamina ply-gaps with gap widths as large as 0.15 in. have been observed in some of the shell specimens. The red-yellow angular patterns in the thickness contour plot correspond to locally thickened regions of the outermost plies of the laminate that develop during the curing process to form outer shell-wall surface ridges. Some of the shell-wall thickness features, such as lamina ply-gaps, are smaller than the imperfection-measurement grid spacing used in this study, and as a result, some of the smaller thickness variation features may not have been included in the measurements. Typical magnified cross-sectional views illustrating the microstructure of typical ply-gaps and outer surface ridges in a composite laminated shell wall are presented in Ref. [12].

Measurements of the top and bottom loading surfaces of the specimens were made every degree around the circumference of the specimens to determine the variation in the shell-end or loading-surface geometry. Typical top and bottom shell-end or loading-surface geometry variations for specimen C3 are denoted by $\delta_{top}(\theta)$ and $\delta_{bot}(\theta)$, respectively, and are shown in Fig. 4. The maximum amplitude of this shell-end or loading-surface variation is approximately 0.0015 inches, which is approximately 4% of t_{ave}

3

or 0.01% of the specimen length.

Test Apparatus and Tests

The specimens were instrumented with electrical resistance strain gages, and direct-current differential transducers (DCDT's) were used to measure displacements. Three non-colinear DCDT's were positioned at three corners of the upper loading platen of the test machine and used to measure the end-shortening displacement Δ and the rotations ϕ_y and ϕ_z of the loading platen as illustrated in Fig. 1. A typical set of measured loading platen rotations is shown in Fig. 5. These results indicate that significant upper platen rotations occur from the onset of loading up to a load value of approximately 6,000 lbs. These rotations are attributed to an initial misalignment of the upper loading platen and the specimen. The rotations of the movable upper loading platen reach a steady state at a load value of 6,000 lbs., and the loading of the specimen, for the most part, continues without additional upper loading paten rotations from 6,000 lbs. up to the buckling or collapse load. During the collapse event, the upper loading platen undergoes an additional amount of rotation.

The specimens were loaded in compression with a 300,000-lb hydraulic universal-testing machine by applying an end-shortening displacement to the shell ends or loading surfaces of the specimens. To help facilitate uniform load introduction into the specimens, the upper loading platen was aligned with the loading surface of the specimen as well as possible before the test by adjusting leveling bolts in the corners of the upper loading platen until strains measured by selected strain gages on the specimens indicated a uniform axial strain distribution in the shell wall.   A shadow moiré interferometry technique was used to observe the shell-wall prebuckling, buckling and postbuckling radial (perpendicular to the shell outer surface) deformation patterns.   All data were recorded with a data acquisition system, and the moiré patterns were recorded photographically and on videotape. The specimens were loaded until general instability or failure of the shells occurred.

Finite-Element Models and Analyses

Nonlinear Analysis Procedure

The shells considered in this study were analyzed with the STAGS (STructural Analysis of General Shells) nonlinear shell analysis code.[13] STAGS is a finite-element code developed for the nonlinear static and dynamic analysis of general shells, and includes the effects of geometric and material nonlinearities in the analysis. The code uses both the modified and full Newton methods for its nonlinear solution algorithms, and accounts for large rotations in a shell by using a co-rotational algorithm at the element level. The Riks pseudo arc-length path-following method[14] is used to continue a solution past the limit points of a nonlinear response. With this strategy, the incrementally applied loading parameter is replaced by an arc-length along the solution path, which is then used as the independent loading parameter. The arc-length increments are automatically adjusted by the program as a function of the solution behavior. The transient analysis option in STAGS uses proportional structural damping and an implicit numerical time-integration method developed by Park.[15] Additional information on the transient analysis procedure can be found in Ref. 16.

The prebuckling, buckling and postbuckling responses of the shells were determined using the following analysis procedure. The prebuckling responses were determined using the geometrically nonlinear quasi-static analysis capability in STAGS. The Riks pseudo arc-length path-following method in STAGS was used to compute the initial shell response until just before buckling occurred. The unstable buckling response of the shell was predicted using the nonlinear transient analysis option of the

code. The transient analysis was initiated from an unstable equilibrium state close to the limit point by incrementing the end displacement by a small amount. An initial time step of 10.0^{-8} seconds was used in the analysis, and the time step was automatically adjusted by the program as a function of the solution behavior. The transient analysis was continued until the kinetic energy in the shell had dissipated to a negligible level, which indicated that the transient response had attenuated. Once the transient analysis had attenuated to a near-steady-state solution, the load relaxation option of the code was used to establish a static equilibrium state. Conventional linear bifurcation buckling analysis results were also determined with STAGS for comparison with the nonlinear response results.

Finite-Element Models

A typical finite-element model of a specimen is illustrated in Fig. 1. The standard 410 quadrilateral element from the STAGS element library was used in the models. The elements of the finite-element mesh are approximately 0.2-in. by 0.2-in. square. Each element has four integration points, which are distributed in such a way as to provide a modeling resolution of approximately 0.1-in. by 0.1-in square. This integration-point spacing is on the order of the measurement- point spacing used when measuring the initial geometric imperfections of the specimens. This highly refined mesh is necessary to model rapidly varying geometric and material parameters such as nonuniform shell-wall thicknesses and lamina stiffness properties. A typical finite-element model contained approximately 120,000 degrees of freedom.

Geometrically perfect and imperfect shells were analyzed in the present investigation. Nominal shell geometry, laminate thickness, lamina mechanical properties, and boundary conditions were used for the finite-element models of the geometrically perfect shells. The nominal boundary conditions consist of setting the circumferential and normal displacements v and w equal to zero in the 1.0-in.-long potted boundary regions of the shell illustrated in Fig. 1, setting $u(L/2,\ \theta) = 0$, and applying a uniform end-shortening $u(-L/2,\ \theta) = \Delta$. The geometrically perfect finite-element models were modified to include the effects of the measured shell imperfections in order to simulate more closely the response of the specimens. These modeling modifications include the effects of the measured initial geometric shell-wall mid-surface imperfections, shell-wall thickness variations, local shell-wall lamina ply-gaps, thickness-adjusted lamina properties, elastic boundary conditions, shell-end geometric imperfections, and nonuniform end loads.

The initial geometric shell-wall mid-surface imperfection $w_o(x,\ \theta)$ is included in the finite-element models by introducing an initial normal perturbation to each node of the mesh by using a user-written subroutine with STAGS for that purpose. The user-written subroutine uses a linear interpolation algorithm that calculates the value of the imperfection for the coordinates of each finite-element node based on the measured shell-wall data.

The shell-wall thickness t, mid-surface eccentricity ecz, and lamina material properties E_1, E_2, G_{12} and ν_{12} are adjusted at each integration point of each element in the finite-element models. The shell-wall mid-surface eccentricity is calculated relative to the average shell-wall mid-surface; that is, $ecz(x,\theta)$ = $-0.5(t_{ave} - t_o(x,\ \theta))$, where t_{ave} and t_o denote the average shell-wall thickness and actual measured thickness, respectively. The lamina properties are adjusted by using the rule of mixtures. In the rule-of-mixtures calculations, it is assumed that any variation in the lamina ply thickness from the nominal thickness is due to a variation in resin volume only, and that the fiber volume remains constant for each ply. However, several assumptions and approximations related to modeling the geometry and stiffnesses of a lamina ply-gap detail were used in the analysis. First, the finite-element models are limited to modeling the shell-wall thickness variation as discrete step-changes and the resolution of the thickness variation is limited by the finite-element integration point spacing (i.e., 0.1 in.).   Results from a study

illustrating the potential effects of these modeling approximations and mesh refinement on the response of a shell with a ply-gap indicate that this modeling approach can affect the predicted response. In particular, it was found that these modeling approximations can lead to an artificial increase or decrease in the size of the measured thickness details, e.g., the width of a lamina ply-gap, resulting in misrepresentation of the local bending stiffnesses and the mid-surface eccentricity of the shell wall at that particular point. In addition, the mesh refinement and integration point spacing used in the present models tend to provide models that are overly stiff in bending by a small amount when they are used for modeling a ply-gap detail. These modeling approximations can have a direct influence on the local bending response of the shell and can result in as much as a 2% variation in the predicted buckling loads. The second assumption is related to the modeling of the stiffnesses of the lamina ply-gap. Two modeling approaches were considered. One approach is to model each ply-gap with a local reduction in thickness, as measured, including the local eccentricity, *ecz*, and reducing the appropriate number of lamina plies in the shell-wall laminate model, hence, reducing the local stiffnesses associated with the local ply-gap detail.

The second approach is to model the ply-gap with the local as-measured reduced shell-wall thickness and the corresponding local mid-surface eccentricity, but assuming that the local thickness reduction is due to a reduction in the resin volume only and, consequently, keeping the fiber volume constant. This approach neglects the local stiffness reduction associated with the ply-gap details. The former modeling approach is very time consuming to implement since it requires the manual definition of each shell-wall laminate associated with each specific ply-gap in the finite-element model. The latter modeling approach is much easier to implement in the model by using a user-written subroutine compatible with the STAGS finite-element analysis code. As a result, the latter modeling approach was used in the present study. Results from a study of this modeling assumption indicate that neglecting the local stiffness reduction associated with a ply-gap would cause only slight differences in the magnitude of the local bending response and no more than a 2% variation in the predicted buckling load for a compression-loaded shell. Moreover, the results of this modeling study indicated that the local shell-wall mid-surface eccentricity is the most important feature of the ply-gap detail for these stability critical problems, and this eccentricity was included in the models for the results presented herein. Results from a numerical parametric study of the effects of ply gaps on the nonlinear and buckling response of compression-loaded cylinders are presented in Ref. [11].

To provide a better simulation of the elastic boundary constraints provided by the potting material at the ends of the specimens, effective axial and radial potting-support stiffnesses were determined for each shell specimen using a two-dimensional generalized plane-strain finite-element analysis of the potting-material–shell-wall detail. The predicted results indicate that the effective axial potted-shell stiffness range from 1.1 to 2.4 times the nominal shell-wall stiffness and the nominal effective radial potting-support stiffness was predicted to be approximately equal to 1.0E5 lbf/in. In the present study the nominal effective axial potted-shell stiffnesses are equal to 1.2, 2.0, 1.3, 1.1, 1.4, and 1.2 times the nominal shell-wall stiffness of shells C1 through C6, repectively. The predicted results also indicate that the increase in the effective axial potted-shell stiffness is inversely proportional to the nominal shell wall stiffness. Details on the boundary stiffness analyses and effects of the boundary stiffness on the response of the shells are given in Ref[12].

Nonuniform end loading of a specimen is attributed to initial specimen-end or loading-surface imperfections and to upper loading-platen rotations that are measured during the experiment. First, the measured upper and lower specimen-end or loading-surface imperfections $\delta_{top}(\theta)$ and $\delta_{bot}(\theta)$, respectively, were included in the finite-element model by introducing an initial in-plane axial perturbation to the nodes at the loaded ends of the shell. Then, the compression load was applied to the shell in two parts.

The nonuniform specimen-end imperfections, $-\delta_{top}(\theta)$ and $-\delta_{bot}(\theta)$, were applied as displacements to the upper and lower ends of the shell, respectively, at the beginning of the analysis to simulate a full contact condition between the shell ends and the loading platens. Then, the experimentally measured end-shortening displacement Δ and upper loading-platen rotations ϕ_y and ϕ_z were applied to the upper shell end or loading surface while holding the lower loading surface fixed as illustrated in Fig. 1; that is, $u(-L/2, \theta) = \Delta + R\cos\phi_y \cos\theta + R\cos\phi_z \sin\theta -\delta_{top}(\theta)$ and $u(L/2, \theta) = -\delta_{bot}(\theta)$.

Failure Analyses

A common Tsai-Wu tensor failure criterion was used to predict material failure in the shells. Two failure criteria were defined and include a delamination failure criteria given by

$$\frac{\tau_{13}^2 + \tau_{23}^2}{S^2} = 1 \tag{1}$$

and an in-plane failure criteria given by

$$\frac{\sigma_1^2 - \sigma_1\sigma_2}{X^2} + \frac{\sigma_2^2}{Y^2} + \frac{\tau_{12}^2}{S^2} = 1 \tag{2}$$

The transverse shear stresses τ_{13} and τ_{23} were approximated using a strength of materials approach which assumes that the transverse shear stress resultant distribution is parabolic through the thickness of the shell wall. The material allowalbles are as follows: longitudinal strength X = 124.0 ksi, transverse strength Y = 8.4 ksi, and shear strength S = 11.6 ksi. When either of the failure indices equals or exceeds a value of one, the material is assumed to have failed. Each stress component of the failure indices is examined to determine the mode of failure. A progressive failure analysis approach was not used in the present study since it was outside the scope of the present study, however, the failure indices were used to indicate the possibility of material failure and to establish failure trends associated with the compression-loaded cylinders considered herein.

Parameter Uncertainty Characterization

Several cylinder parameter values exhibit a significant amount of uncertainty and an attempt to characterizes these uncertainties and include them in the present analyses was made. The cylinder parameter uncertainties considered include uncertainties in geometric imperfection measurements, lamina fiber volume fraction, fiber and matrix properties, applied end load distribution, and boundary conditions.

Imperfection measurement uncertainty is attributed to the accuracy tolerances of the coordinate measurement device used to measure the shell wall geometry and end-surface imperfection and this tolerance is equal to ± 0.0006 inches. This tolerance corresponds to less than 0.01% uncertainty in the shell-wall imperfection measurement (e.g., Fig. 2). In contrast, the measurement tolerance corresponds to a ±3.0% uncertainty in the thickness measurement (e.g., Fig. 3) and approximately ±6% uncertainty in the shell-end imperfection measurement (e.g., Fig. 4).

The extent of uncertainty in fiber and matrix properties and fiber volume fraction were characterized using published data contained in Volume 2 of the MIL 17 Handbook and from the material manufacturer. It was determined that the nominal fiber and matrix properties can vary ±5% and the nominal fiber volume fraction can vary ±3%. The nominal fiber properties used in the present study are

7

as follows: longitudinal modulus of 31.19 Msi, transverse modulus of 3.49 Msi, shear modulus of 1.81 Msi, and Poisson's ratio of 0.27. The nominal matrix properties are as follows: Young's modulus of 0.53 Msi, shear modulus of 0.22 Msi, and Poisson's ratio of 0.35. The nominal fiber volume fraction is equal to 0.62.

Applied load distribution uncertainty is attributed to shell end-surface imperfection uncertainty and uncertainty in the orientation of the loading platen with respect to shell-ends or loading surfaces of the cylinder specimen during the test. Applied load distribution uncertainties are characterized indirectly by comparing the measured and predicted axial strains at selected points near the top and bottom loading surfaces of the shell. A correction to the applied displacement distribution was determined from the differences in the measures and predicted strains as follows. A user-written program external to the STAGS code was used to analyze the differences in the measured and predicted strains for a specified applied load value. This program used an iterative predictor-corrector method to determine a correction to the applied shell-end displacements. A new finite-element model was conducted with this displacement correction included in the model. This process was repeated iteratively until the difference in the predicted and measured strains reached a predetermined tolerance. A typical predicted displacement correction is presented in Ref. [12] and the amplitude of the displacement correction is on the order of ±0.0005 in.

Boundary condition uncertainty is attributed to uncertainties in the potting material stiffness and uncertainty in the integrity of the bond between the potting material and the shell wall. Visual inspection of the specimens before and after testing indicated that the potting material has a tendency to separate from the shell wall. This boundary condition uncertainty was not rigorously characterized, however, results from several numerical experiments indicate that variations in the boundary stiffness can have a significant effect on the displacement and strain response near the shell ends and effect the character of the collapse response of the shells, e.g., Ref. [12]. Therefore, it was arbitrarily assumed that the effective axial and radial boundary stiffnesses might vary ±10%.

Results and Discussion

Numerically predicted and experimentally measured results for the six compression-loaded graphite-epoxy cylindrical shells considered in this study are presented in this section. The shell-wall laminates of the six shells include four different orthotropic laminates and two different quasi-isotropic laminates. The 8-ply shells, C1- C3, have shell-radius-to-thickness ratios equal to 200 and the 16-ply shells, C4 - C6, have shell-radius-to-thickness ratios equal to 100. The predicted results were obtained from finite-element models of geometrically perfect shells and shells that include initial geometric shell-wall mid-surface imperfections, shell-wall thickness variations and thickness-adjusted lamina properties, local shell-wall lamina ply-gaps, elastic boundary support conditions, and nonuniform loading effects. In addition, uncertainties in geometric and material properties, loading distribution, and boundary conditions were included in the analyses. These results are presented to illustrate the overall behavior of compression-loaded graphite-epoxy shells and the effects of imperfections and parameter uncertainties on their response. First, results illustrating a typical nonlinear response of a compression-loaded quasi-isotropic 8-ply shell are presented. Then, comparisons between selected numerically predicted results and experimentally measured results for the 8-ply and 16-ply shells are presented. The results include predicted and measured load–end-shortening response curves, predicted prebuckling, buckling and postbuckling deformation response patterns, predicted axial and circumferential stress resultant patterns, and predicted material failures. The six composite shells considered in this study are interchangeably referred to herein as shells or specimens C1 through C6.

Typical Nonlinear Response of an Imperfect Compression-loaded Cylindrical Shell

Results from a nonlinear analysis of an imperfect compression-loaded 8-ply $[\mp 45/0/90]_s$ quasi-isotropic cylindrical shell C3 are presented in this section. The nonlinear analysis results are from a shell model that includes the effects of the measured initial shell-wall geometric and thickness imperfections, thickness-adjusted material properties, measured loading variations, and elastic radial support conditions. The predicted load-shortening response of shell C3 is shown in Fig. 6a. The axial load P and end-shortening Δ are normalized with respect to the linear bifurcation buckling load of the geometrically perfect nominal shell, P_{bif} = 42.59 Kips, and the nominal shell-wall thickness, t = 0.04 in, respectively. The load–end-shortening curve indicates a linear prebuckling response. The general instability occurs at a normalized axial load level of P/P_{bif} = 0.977, marked by the letter A. The general instability response is followed by a sudden reduction in the axial load supported by the shell and is associated with the transient collapse response of the shell. The corresponding load-time history of the transient collapse response is shown in Fig. 6b. The load-time history curve exhibits a sudden reduction in axial load until the collapse response attenuates and the axial load achieves a steady-state value. The kinetic energy in the shell obtains a maximum value during the transient collapse response and dissipates over time and the shell reaches a stable postbuckling equilibrium state after approximately 0.007-0.008 seconds. The shell exhibits postbuckling load carrying capacity, however, the effective axial stiffness of the specimen is significantly reduced in the postbuckling range of loading as indicated by the reduction in the slope of the load-shortening response curves. This reduction in effective axial stiffness is caused by large magnitude radial deformations that develop in the specimen during buckling which result in significant load redistribution in the specimen and reduces the effective, load-carrying cross-section of the cylinder

The transient deformation responses for selected time steps during the transient collapse response of shell C3, indicated by the letters A through F in Figs. 6a and 6b, are presented in Fig. 7a through 7f, respectively. Just before buckling occurs, the shell wall deformations are characterized by several localized ellipse-like buckles as indicated in Fig. 7a. The localization in the deformation pattern is caused by the combination of a local geometric shell-wall imperfection that is in the form of a significant variation in the shell-wall mid-surface geometry, and the intersection of a helical ply-gap and a circumferentially aligned ply-gap in the shell at x/L_T = 0.25 and θ = 210°. The localized deformations occur in regions with destabilizing compressive axial and circumferential stresses. After approximately 0.0012 seconds have elapsed in the transient response, a single ellipse-like buckle has grown in amplitude and couples with the destabilizing stresses in the shell wall to cause the general instability and collapse of the shell. The magnitude of the shell-wall radial displacement varies between ±0.5 times the shell-wall thickness. After additional time has elapsed in the transient collapse response, additional local buckles have formed around the circumference and along the length of the shell as indicated in Fig. 7c, and the normalized axial load has decreased from 0.974 to 0.759. The magnitude of the shell-wall radial displacement varies between +2 to -4 times the shell-wall thickness. As the buckling process continues, the normalized axial load has decreased further to 0.554 and the deformation pattern in the shell wall continues to evolve and additional ellipse-like buckles have formed around the circumference of the shell as indicated in Fig. 7d. In addition, some of the buckles in the shell begin to coalesce into larger diamond-shaped buckles. The magnitude of the shell-wall radial displacement varies between +3 to -7 times the shell-wall thickness. After approximately 0.01 seconds have elapsed in the transient response, the kinetic energy in the shell has dissipated to a negligible level indicating that the transient response has attenuated, and the shell has deformed into a stable postbuckling mode-shape as indicated in Fig. 7e. As loading continues in postbuckling region, the diamond-shaped buckles increase in size and the magnitude of the radial deformations of the buckles and the outer-surface ridges increase to between +4 and -9 times

9

the shell-wall thickness as shown in Fig. 7f.

Numerically predicted prebuckling, transient buckling, and postbuckling axial and circumferential membrane stress contours of the imperfect quasi-isotropic shell C3 are presented in Figs. 8a, 8b, and 8c, respectively. Just before buckling occurs, the stress distributions are nonuniform and exhibit several localized regions of biaxial compression stress in the bending boundary near the ends of the shell as shown in Fig. 8a. In particular, compressive axial an circumferential membrane stresses occur in the shell at $x/L_T = 0.25$ and $\theta = 210^o$ and these stresses couple with the local bending deformations in the shell wall to cause the general instability and collapse of the shell. During the transient collapse of the shell the axial load decreases rapidly and a significant redistribution of the stresses in the shell occurs. For example, at time = 0.0024 seconds and $P/P_{bif} = 0.554$, redistribution of the axial and circumferential membrane stresses occurs and high-magnitude, localized stress concentrations develop near the buckles in the shell wall as indicated in Fig. 8b. More specifically, the axial stress distribution exhibits a significant unloading of the shell near the center of the buckles and the majority of the axial compression load in the buckled region of the shell is supported by the ridges between the adjacent buckles. In addition, the results indicate a significant increase in the magnitude of the circumferential compression stresses in the buckles with the maximum value of the compressive stress increasing from -240 lbf/in. to -430 lbf/in., as compared to the initial buckling stresses shown in Fig. 8a. The results indicate that, in the postbuckling configuration, the shell exhibits significant membrane stress redistribution throughout the entire shell. For example, at $\Delta/t = 1.3$ and $P/P_{bif} = 0.554$, the results indicate that the majority of the axial compression load is supported by the ridges between adjacent buckles in the shell wall as shown in Fig. 8c. In addition, alternating bands of circumferential tension and compression membrane stresses are present in the shell. However, the magnitude of the maximum axial and circumferential in the postbuckling configuration shown in Fig. 8c are 18.5 and 23.2% lower than the corresponding stresses during the transient collapse response shown in Fig. 8b. This result indicates that the maximum stresses during the buckling process are not necessarily obtained in the stable postbuckling configuration, rather, the large magnitude displacement gradients and internal stress redistribution can cause higher stresses to occur in the shell during the transient collapse process. Similar results were obtained for the other shells considered and indicated similar response characteristics.

Corresponding numerical results presented in Ref. [12] indicate that the deformation and internal stress response of a compression-loaded geometrically perfect idealized shell is characterized by a uniform axisymmetric prebuckling response and uniform asymmetric transient buckling and postbuckling response. These results are in contrast to the present results in which the prebuckling and initial transient buckling responses of the imperfect shells are characterized by nonuniform localized behavior caused by the coupling of localized imperfections and stresses in the shell. Results from a numerical parametric study illustrating the nonlinear coupling between selected imperfections and its effects on the buckling load of a compression-loaded quasi-isotropic cylindrical shell is discussed in Ref [12].

Numerically predicted prebuckling, transient buckling, and postbuckling material failure contours of the imperfect quasi-isotropic shell C3 are presented in Figs. 9a, 9b, and 9c, respectively. The contour plots correspond to the values of the failure indices for delamination failures, FI-1, and in-plane fiber or matrix, FI-2, defined in Eqs. 1 and 2, respectively. Material failure is assumed when the failure index equals or exceeds a value of one. Incipient to buckling, both failure indices are less than one indicating no material failure occurs during the prebuckling response of the shell as shown in Fig. 9a. However, during the transient collapse response the in-plane fiber/matrix failure index FI-2 exceeds a value of one as shown in Fig. 9b, and indicates a potential for failures to occur in regions of large magnitude displacement gradients and large magnitude compressive membrane stresses in the shell wall, e.g., see Fig.8b. The material failures are characterized by matrix compression failures. The results indicate that,

in the postbuckling configuration, delamination failures and in-plane matrix and fiber compression failures are predicted to occur along the ridges between the adjacent buckles in the shell wall (sometimes referred to as nodal lines) as shown in Fig. 9c. These results are consistent with the observed failures in the test specimens. Similar results were obtained for shells C1 and C2 and indicated similar failure characteristics.

Predicted and Measured Response Comparisons

Selected results from nonlinear analyses of the six compression-loaded cylindrical shells are compared to the experimentally measured results in this section. The nonlinear analysis results are for shell models that include the effects of the measured initial geometric and thickness imperfections, thickness-adjusted material property variations, measured loading variations, elastic radial support conditions, and selected specimen parameter uncertainties. The specimen parameter uncertainties considered include uncertainty in the imperfection measurement accuracy, fiber and matrix properties, fiber volume fraction, applied load, and boundary stiffness, as characterized in an earlier section. Upper and lower response bounds were determined based upon the results of a traditional combinatorial analysis of the effects the selected parameter uncertainties. Predicted and measured load–end-shortening response curves and postbuckling displacement contours are presented in this section. In addition, typical numerically predicted prebuckling, buckling, and postbuckling displacement contours, axial and circumferential stress contours, and failure index contours are presented for imperfect 8-ply and 16-ply quasi-isotropic shells.

8-ply Shells Three sets of numerically predicted and experimentally measured load–end-shortening response curves for the 8-ply shells; C1 [∓45/0$_2$]$_s$, C2 [∓45/90$_2$]$_s$, and C3 [∓45/0/90]$_s$, are shown in Fig. 10. The axial load P is normalized by the quantity EA, i.e., the effective axial stiffness of the shell, denoted by E, multiplied by the nominal shell cross-sectional area, denoted by A, and the end-shortening Δ is normalized by the nominal shell length $L = 16.0$ in. The solid and dashed lines in the figure represent experimentally measured and numerically predicted results, respectively. Each shell has two predicted response curves representing predicted upper and lower bounds to the response based on specimen parameter uncertainties and the regions between the response bounds are shaded for clarity. The measured buckling point of each shell is marked by a filled circle and the ultimate failure of each shell is marked with an **X**. In addition, each shell has one or more numerically predicted failure boundaries represented by the dark grey solid lines in the figure. Each failure boundary is labeled with the number 1, 2, or 3, and denotes matrix failure initiation, fiber failure initiation, and delamination failure initiation, respectively. The measured results indicate that the prebuckling responses are linear up to the general instability point indicated in the figure for each specimen. General instability occurs at normalized load levels of $P/EA = 0.00122$, 0.0044, and 0.0022 for specimens C1, C2, and C3, respectively, and are 7.8, 13.7, and 17.6% lower than the predicted linear bifurcation buckling loads for the corresponding geometrically perfect, nominal shells, respectively. The general instability points are followed by a sudden and significant reduction in the axial load supported by the specimens and is associated with the unstable transient collapse response of the specimens. During collapse, the specimens buckled into the classical diamond-shaped general instability mode-shape and the collapse response was accompanied by an audible snapping sound. In addition, no significant visible failures were observed in the specimen as a result of the collapse response. The specimens obtained stable postbuckling equilibrium state and exhibited additional loading carrying capacity in the postbuckling range. Additional audible popping sounds were heard during the loading of the specimens in the postbuckling range suggesting a progressive accumulation of material failures in the specimens and the accumulation of material failures continued until the ultimate failure of the specimen occurred. In addition, the progressive accumulation of material damage in the specimens may account for the discontinuous jumps in the load-shortening response curves shown in Fig. 10. The results in Fig. 10 indicate that, for the most

part, the measured responses fall within the numerically predicted response bounds. In particular, the results indicate that the measured response curves tend to correlate with the mid-point between the upper and lower predicted response bounds. The predicted results indicate that, in most cases, material failure in the specimens is likely to occur at load levels near the general instability point and in the postbuckling range of loading. More specifically, matrix compression failure is predicted to occur in shell specimens C2 and C3 near the general instability point, followed by fiber compression failures and delamination type failures in the postbuckling range of loading. In contrast, the numerical results predict matrix and fiber compression failures to occur in specimen C1 in the postbuckling range of loading only. These failure predictions correlate well with the failure trends observed in the tests.

Predicted initial post-collapse radial displacement contours and the corresponding observed moiré fringe patterns for specimen C1 are shown in Fig. 11. The dashed contour lines in the predicted displacement contour plots represent inward displacements and the solid lines represent outward displacements. The density of the contour lines indicates the severity of the displacement gradients in the specimen. These results indicate that the specimen collapses into a general-instability diamond-shaped buckling pattern with 16 half-waves around the circumference and one half-wave along the length, as predicted by the finite-element analysis. However, the numerical results predict that the mode-shape pattern is 15-20° out-of-phase with the observed mode-shape pattern. Predicted initial post-collapse normal displacement contours and the corresponding observed moiré fringe patterns for specimen C2 are shown in Fig. 12. These results indicate that the specimen collapses into a general instability diamond-shaped buckling pattern with 14 half-waves around the circumference and two half-waves along the length, as predicted by the finite-element analysis. In addition, the predicted mode-shape is in-phase with the observed mode-shape. Similar results for shell C3 indicate that the shell collapses into a general-instability diamond-shaped pattern with 16 circumferential half-waves and two axial half-waves. However, the analytical results predicted that the mode-shape pattern is approximately 15° out-of-phase with the observed moiré fringe pattern.

16-ply Shells Numerically predicted and experimentally measured load–end-shortening response curves for the 16-ply shells C4 through C6 are shown in Fig. 13. The axial load P is normalized by the quantity EA, i.e., the effective axial stiffness of the shell, denoted by E, multiplied by the nominal shell cross-sectional area, denoted by A, and the end-shortening Δ is normalized by the nominal shell length $L = 16.0$ in. The solid and dashed lines in the figure represent experimentally measured and numerically predicted results, respectively. Each shell has two predicted response curves representing predicted upper and lower bounds to the response based on specimen parameter uncertainties and the regions between the response bounds are shaded for clarity. The measured buckling point of each shell is marked by a filled circle and the ultimate failure of each shell is marked with an **X**. In addition, each shell has one or more numerically predicted failure boundaries represented by the dark grey solid lines in the figure. Each failure boundary is labeled with the number 1, 2, or 3, and represents matrix failure initiation, fiber failure initiation, and delamination failure initiation, respectively. The measured results indicate that the initial load-shortening responses are, for the most part, linear up to the limit load for each specimen as indicated in the figure. However, the load-shortening responses for specimens C5 and C6 exhibit slight nonlinear behavior at end-shortening levels greater than $\Delta/L = 0.004$. General instability occurs at normalized load levels of $P/EA = 0.0027$, and 0.0049 for specimens C4, and C6, respectively, and are 16.8, and 18.4% lower than the predicted linear bifurcation buckling loads for the corresponding geometrically perfect, nominal shells, respectively. The results show that the general instability points of specimens C4 and C6 coincide with the ultimate failure of the specimens and the specimens do not exhibit postbuckling load carrying capacity. More specifically, experimental results indicated that, upon collapse, specimens C4 and C6 exhibited a significant amount of material failure including fiber and matrix compression failures and delamination failures, and these material failures caused the ultimate or complete failure of the

specimens. The predicted results indicate that, in most cases, the initiation of material failure is likely to occur during the initial portion of the transient collapse response as shown in Fig. 13 and these results explain the observed failure trends in specimens C4 and C6. In contrast, specimen C5 does not exhibit a general instability point, rather, the specimen exhibits complete failure at a load level of *P/EA* = 0.0062, and is 43.9% lower than the predicted linear bifurcation buckling load for the corresponding geometrically perfect, nominal shell. The complete or overall failure of the specimen is characterized by a significant amount of delamination failures and fiber and matrix compression failures around the entire circumference of the shell. Post-test inspection of the specimen indicated that the overall failure of the shell may have been initiated by a material failure near an axially aligned ply-gap in the cylinder wall.

Numerically predicted results of the prebuckling, transient buckling, and postbuckling deformation and internal stress responses were obtained for the 16-ply shells and indicated similar response trends to those presented for the 8-ply quasi-isotropic shell in Figs. 7 and 8. In particular, the results indicate that the prebuckling responses in the shells are characterized by localized displacement and internal stress distributions. The localized shell-wall deformations couple with destabilizing stresses in the shell to cause the general instability and collapse of the shell. In general, the localized deformations and stress distributions are caused by the combination of local geometric shell-wall geometric and thickness imperfections, material property variations, and shell-end-loading nonuniformities.

Predicted initial post-collapse radial displacement contours and the corresponding observed displacement response for specimen C4 are shown in Figs. 14a and 14b. The dashed contour lines in the predicted displacement contour plots represent inward displacements and the solid lines represent outward displacements. The density of the contour lines indicates the severity of the displacement gradients in the specimen. These results indicate that the specimen collapses into a general-instability diamond-shaped buckling pattern with 16 half-waves around the circumference and one half-wave along the length, as predicted by the finite-element analysis. The numerical results predict that the mode-shape pattern is in phase with the observed mode-shape pattern. In addition, the specimen exhibits a significant amount of damage near the ridges between the adjacent buckles in the shell wall. The material failures include fiber and matrix compression failures and delamination type failures. These failures are consistent with the predicted material failures in the shell. In particular, the numerical results indicate that, incipient to buckling, the in-plane fiber/matrix failure index FI-2 exceeds a value of one and indicates that matrix compression failures are likely to occur in the bending boundary regions of the shell. During the transient collapse response the delamination failure index FI-1 and the in-plane fiber/matrix failure index FI-2 exceed a value of one and indicate a potential for significant failures to occur. More specifically, the results indicate that fiber and matrix compression failures and delamination type failures may occur in regions of large magnitude displacement gradients and large magnitude membrane compression stresses and transverse shear stresses associated with the ridges that form between adjacent buckles in the shell wall. Similar results were obtained for specimen C6 and indicate similar failure trends. Predicted initial post-collapse normal displacement contours and the corresponding observed displacement response for specimen C5 are shown in Fig. 15a and 15b. The observed material failures in specimen C5 are clearly visible in Fig. 15a   In addition, a 0.15-in-wide ply-gap is shown in the figure and the overall failure of the shell may have been initiated by a material failure near this ply-gap. Numerical results illustrating the effects of a ply-gap on the internal stress distribution in the shell wall are presented in Ref. [12]. The results indicate that the ply-gap can cause significant stress concentrations to develop within the laminate and that the stress levels can equal or exceed the stress allowables for the material at relatively low applied load levels. In particular, predicted membrane compression stress and transverse shear stress values at buckling can be on the order of two to three times the allowable values for the material. These results suggest that delamination failures and fiber and matrix compression failures may occur near ply gaps in the shell wall for load values less than the predicted buckling load of the shell.

Concluding Remarks

The results of an experimental and analytical study of the effects of imperfections on the nonlinear response and buckling loads of unstiffened thin-walled compression-loaded graphite-epoxy cylindrical shells with six shell-wall laminates are presented. The shell-wall laminates considered in this study include two quasi-isotropic laminate and four different orthotropic laminates. Shell-radius-to-thickness ratios equal to 100 and 200 were also considered. Numerical results for the nonlinear prebuckling, transient buckling, and post-buckling response of shells with measured imperfections are presented. The numerical results include the effects of traditional initial geometric shell-wall mid-surface imperfections and the effects of other nontraditional imperfections. These nontraditional imperfections include shell-wall thickness variations, material property variations, shell-end geometric imperfections, local shell-wall ply-gaps associated with the fabrication process, variations in loads applied to the end of the shell, and elastic boundary support conditions. In addition, upper and lower bounds to the nonlinear response of the shells are presented which were determined from a combinatorial analysis of the effects of uncertainties in several shell parameters. The uncertainties considered in the present study include uncertainties in the geometric imperfection measurements, lamina fiber volume fraction, lamina fiber and matrix properties, boundary conditions, and applied load distribution. A high-fidelity nonlinear shell analysis procedure has been used to predict the nonlinear response and failure of the shells, and the analysis procedure accurately accounts for the effects of these traditional and nontraditional imperfections and parameter uncertainties on the nonlinear response and failure of the shells. The analysis results generally correlate well with the experimental results indicating that it is possible to predict accurately the complex nonlinear response, buckling loads, and failure for compression-loaded composite shell structures.

The numerical results indicate that the effects of the traditional and nontraditional imperfections, and selected parameter uncertainties considered in this study can be important for predicting the buckling loads of composite shells since they can significantly affect the nonlinear response and buckling loads of the shells. The results indicate that the measured imperfections can couple with the in-plane compressive stress resultants in a nonlinear manor to affect the shell response. In particular, typical results that illustrate the response of a compression-loaded quasi-isotropic shell were presented and indicated that a complex nonlinear interaction between localized shell-wall prebuckling deformations in the bending boundary region of the shell and compressive axial and circumferential stresses caused the overall buckling of the shell to occur. The localized deformations were caused by the combination of a local geometric shell-wall imperfection that was of the form of a significant variation in the shell-wall mid-surface geometry, and the intersection of a helical ply-gap and a circumferentially aligned ply-gap in the shell wall.

The numerically predicted and experimentally measured results indicate that the 8-ply shells considered in this study exhibit linear prebuckling responses followed by a general instability response. The general instability response corresponds with the overall collapse of the shell in which the shell exhibits a significant reduction in axial load carried by the shell and the shell wall deforms into a classical diamond-shaped general instability mode-shape and have significant postbuckling load carrying capacity. The shells exhibited significant material failures in the postbuckling region of loading and a progressive accumulation of these material failures caused the ultimate failure of the shells. The material failures in the shell included matrix and fiber compression failures and delamination type failures and the material failures typically occurred in regions of large magnitude displacement gradients and large magnitude compressive membrane stresses and transverse shear stresses in the shell wall. In contrast, the 16-ply shells exhibited significant material failures upon buckling and had no postbuckling load carrying capacity. More specifically, as the 16-ply shells buckled, the internal stresses exceeded the allowable stresses levels of the material and caused the overall failure of the shell. In one case, however, a 16-ply

specimen exhibited premature failure during the test. The overall failure of the specimen was characterized by significant fiber and matrix compression failures and delamination type failures around the circumference of the specimen. Post-test inspection of the shell indicated that the overall failure of the specimen may have been initiated by a material failure near an axially aligned ply-gap in the specimen wall.

The results indicate that, for the most part, the measured response of the shells falls mid-way between the predicted upper and lower bounds to the response. In addition, numerically predicted material failure initiation agreed well with experimentally observed failure trends. These results indicate that the nonlinear analysis procedure used in this study can be used to determine accurate, high-fidelity design knockdown factors and response bounds that can be used for predicting composite shell buckling and failure loads in the design process. The traditional and nontraditional imperfections considered in this study could be used to formulate the basis for a generalized imperfection signature of a composite shell that includes the effects variations or uncertainties in the shell-geometry, fabrication-process, load-distribution and boundary stiffness parameters. The high-fidelity nonlinear analysis procedure used in this study can be used to form the basis for a shell analysis and design approach that includes this generalized imperfection signature and addresses some of the critical shell-buckling design criteria and design considerations for composite shell structures without resorting to the traditional empirical shell design approach that can lead to overly conservative designs. Since the nonlinear analysis procedure can be used to predict local shell-wall stresses and strains at any point in the shell load-response history, the analysis procedure can also be used to form a robust failure analysis for composite shell structures with nonlinear response characteristics.

References

1. Anon., Buckling of Thin-Walled Circular Cylinders. NASA Space Vehicle Design Criteria, NASA SP-8007, September 1965.

2. Koiter, W. T., "On the Stability of Elastic Equilibrium," (in Dutch), H. J. Paris, Amsterdam, Holland, 1945; translation available as AFFDL-TR-70-25, February 1970, Wright-Patterson Air Force Base.

3. von Kármán, T. and Tsien, H-S., "The Buckling of Thin Cylindrical Shells Under Axial Compression," Journal of the Aeronautical Science, Vol. 8, No. 8, June 1941, pp. 303-312.

4. Budiansky, B. and Hutchinson, J., "Dynamic Buckling of Imperfection Sensitive Structures," Proceedings of the 11th IUTAM Congress, H. Gortler, Ed., Springer-Verlag, Berlin, 1964, pp. 636-651.

5. Árbocz, J. and Babcock, C. D., "The Effect of General Imperfections on the Buckling of Cylindrical Shells," Journal of Applied Mechanics, Vol. 36, Series E, No. 1, 1969, pp. 28-38.

6. Sechler, E. E., "The Historical Development of Shell Research and Design," in Thin-Shell Structures, Theory, Experiments and Design, Fung, Y. C. and Sechler, E. E., Eds., Prentice-Hall, Englewood Cliffs, NJ, 1974, pp. 3-25.

7. Árbocz, J., "The Effects of Imperfect Boundary Conditions on the Collapse Behavior of Anisotropic Shells," Proceedings of the Joint Applied Mechanics and Materials ASME Summer Conference, AMD-MD'95, Los Angeles, CA, June 28-30, 1995.

8. Árbocz, J., Starnes, J. H., Jr., and Nemeth, M. P., "A Hierarchical Approach to Buckling Load Calculations," Proceedings of the 40th AIAA/ASME/ASCE/AHS/ASC Structures, Structural Dynamics, and Materials Conference, St. Louis, MO, 1999. AIAA Paper No. 99-1232, April 1999.

9. Koiter, W. T., Elishakoff, I., Li, Y. W., and Starnes, J. H., Jr., "Buckling of an Axially Compressed Imperfect Cylindrical Shell of Variable Thickness," Proceedings of the 35th AIAA/ASME/ASCE/AHS/ASC Structures, Structural Dynamics and Materials Conference, Hilton Head, SC, 1994. AIAA Paper No. 94-1339, April 1994.

10. Starnes, J. H., Jr., Hilburger, M. W., and Nemeth, M. P., "The Effects of Initial Imperfections on the Buckling of Composite Shells," Composite Structures: Theory and Practice, ASTM STP 1383, P. Grant and C. Q. Rousseau, Eds., American Society for Testing and Materials, 2000, pp. 529-550.

11. Hilburger, M. H., and Starnes, J. H., Jr., "Effects of Imperfections on the Buckling Response of Compression-loaded Composite Shells," Proceedings of the 41st AIAA/ASME/ASCE/AHS/ASC Structures, Structural Dynamics, and Materials Conference, Atlanta, GA, 2000. AIAA Paper No. 2000-1387, April 2000.

12. Hilburger, M. H., and Starnes, J. H., Jr., "High-fidelity Analysis of Compression-loaded Composite Shells," Proceedings of the 42nd AIAA/ASME/ASCE/AHS/ASC Structures, Structural Dynamics, and Materials Conference, Seattle, WA, 2001. AIAA Paper No. 2001-1394, April 2001.

13. Rankin, C. C., Brogan, F. A., Loden, W. A., and Cabiness, H. D., "STAGS Users Manual, Version 3.0," Lockheed Martin Missiles & Space Co., Inc., Advanced Technology Center, Palo Alto, CA, Report LMSC P032594, 1999.

14. Riks, E., "Progress in Collapse Analysis," Journal of Pressure Vessel Technology, Vol. 109, 1987, pp. 27-41.

15. Park, K. C., "An Improved Stiffly Stable Method for Direct Integration of Nonlinear Structural Dynamics," Journal of Applied Mechanics, Vol. 42, June 1975, pp. 464-470.

16. Riks, E., Rankin, C. C., and Brogan, F. A., "On the Solution of Mode Jumping Phenomena in Thin-walled Shell Structures," Computer Methods in Applied Mechanics and Engineering, Vol. 136 (1-2), 1996, pp. 59-92.

17. Fuchs, J. P., Hyer, M. W., and Starnes, J. H., "Numerical and Experimental Investigation of the Bending Response of Thin-Walled Composite Cylinders," Virginia Polytechnic Institute and State University, Center for Composite Materials and Structures, Report CCMS-93-19/VPI-E-93-11, September 1993.
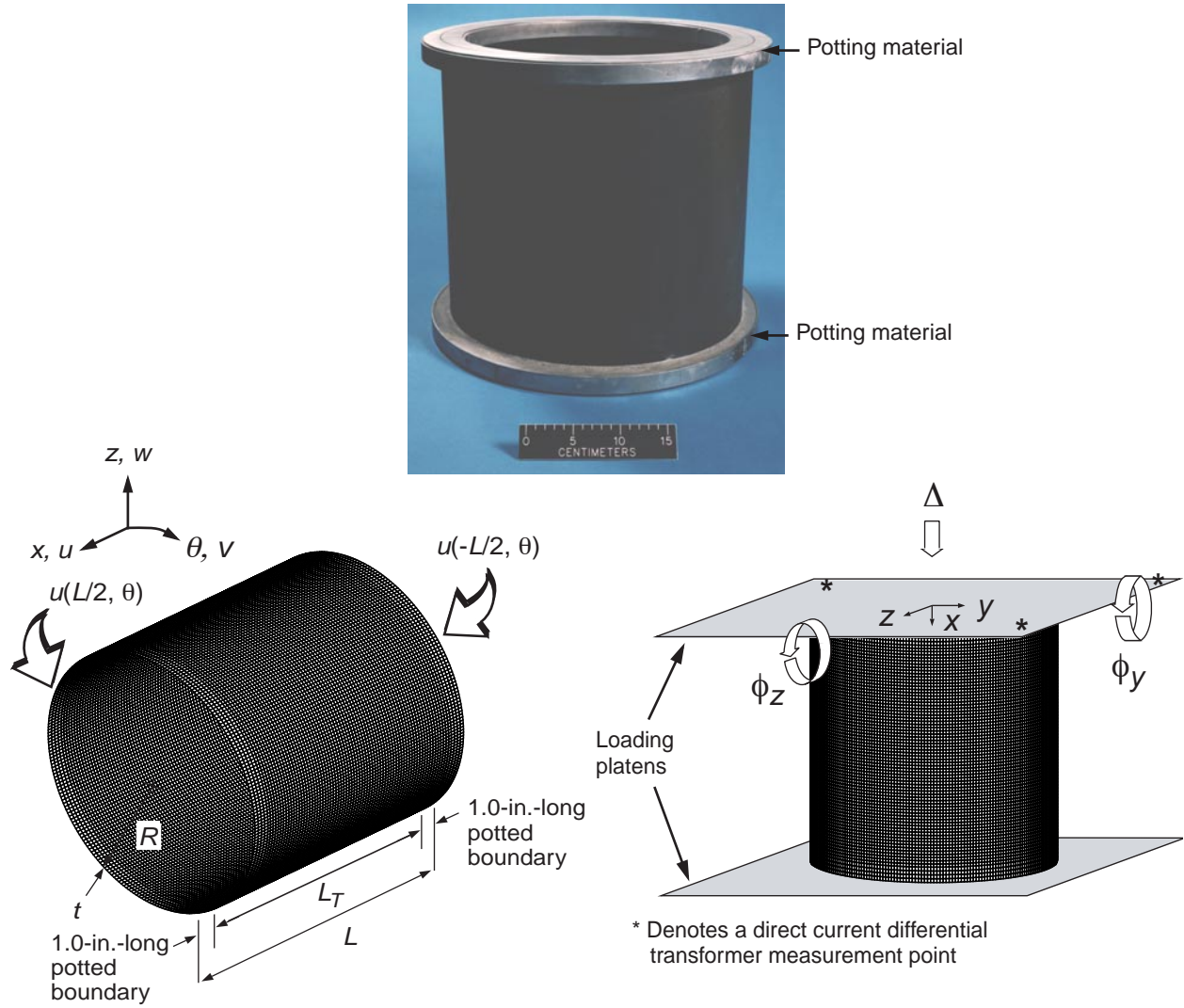
Fig. 1 Typical specimen, finite-element model geometry and loading conditions.
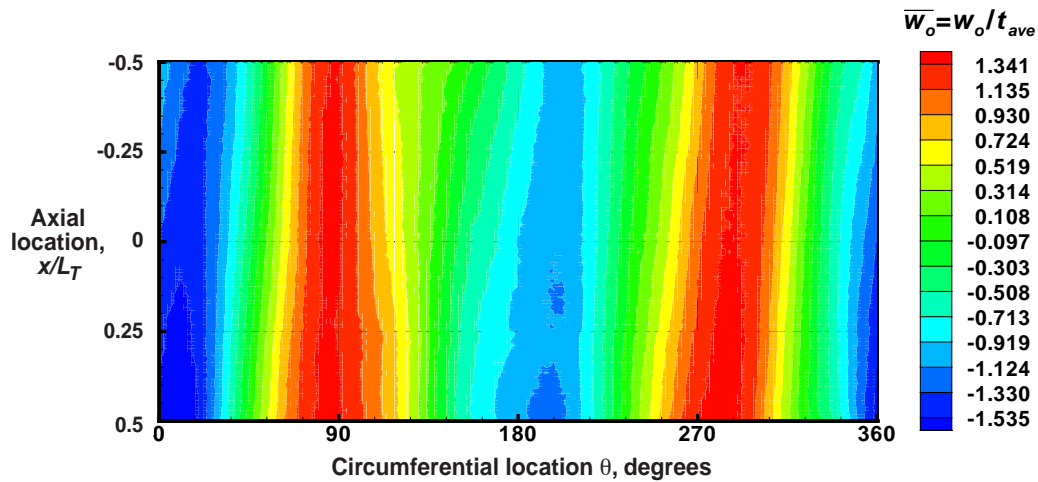
Fig. 2 Typical measured inner-surface imperfection shape for shell specimen C3.
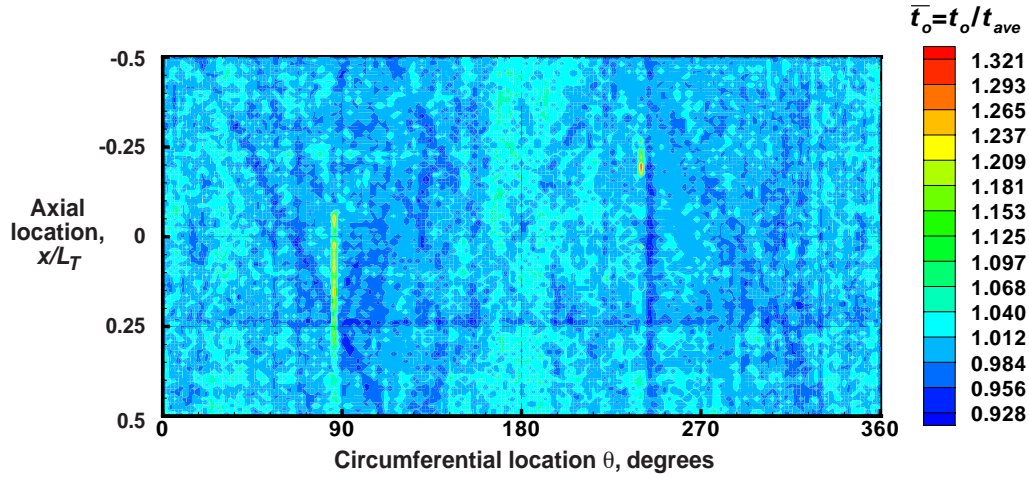
Fig. 3 Typical measured wall thickness variation for a shell specimen C3.
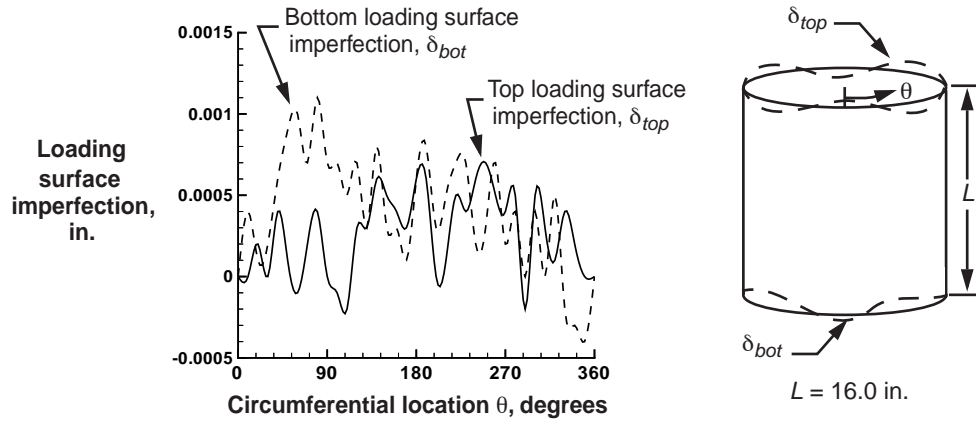
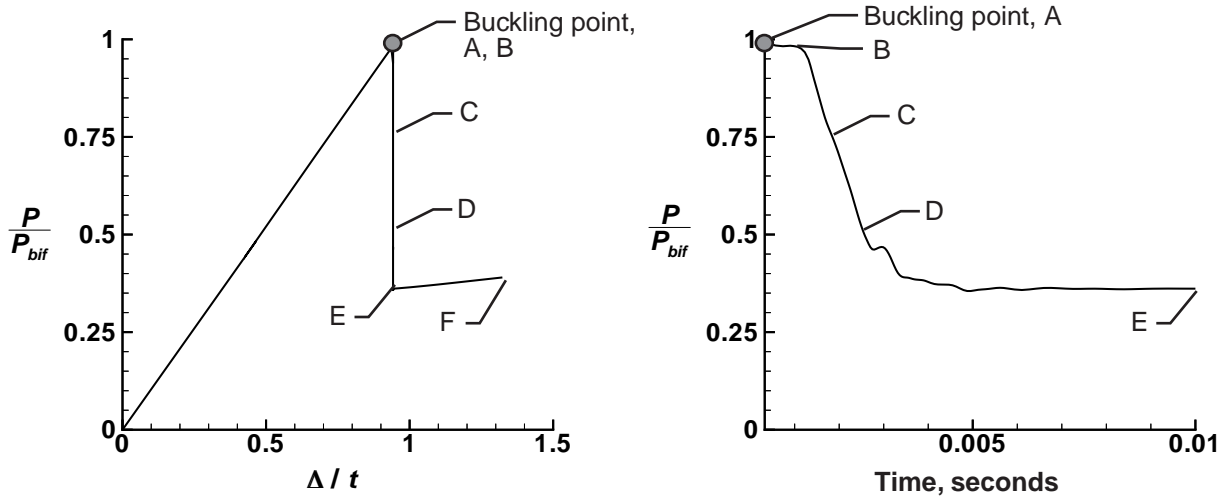**Fig. 4 Typical measured shell-end or loading-surface imperfections for a shell specimen C3.**
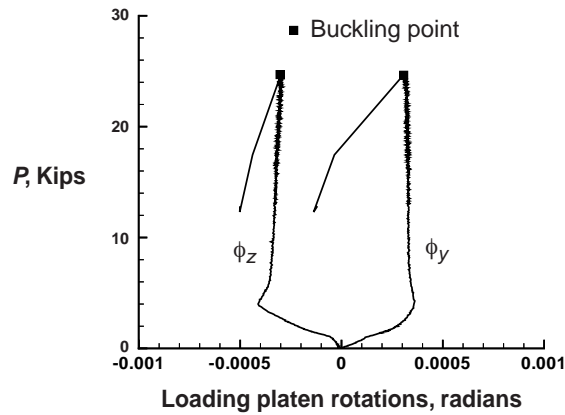
Fig. 5 Typical experimentally measured loading platen rotations.

a) Normalized load–end-shortening response curve   b) Normalized load-time history during collapse

Fig. 6 Numerically predicted response of an imperfect, compression-loaded, quasi-isotropic shell C3.

a) Prebuckling deformations
Time = 0.0 seconds
$\Delta/t = 0.93$
$P / P_{bif} = 0.977$

b) Initial buckling deformations
Time = 0.0012 seconds
$\Delta/t = 0.94$
$P / P_{bif} = 0.974$

c) Transient buckling deformations
Time = 0.0019 seconds
$\Delta/t = 0.94$
$P / P_{bif} = 0.759$

d) Transient buckling deformations
Time = 0.0024 seconds
$\Delta/t = 0.94$
$P / P_{bif} = 0.554$

e) Initial post-buckling deformations
Time = 0.01 seconds
$\Delta/t = 0.94$
$P / P_{bif} = 0.364$

f) Post-buckling deformations
$\Delta/t = 1.3$
$P / P_{bif} = 0.390$
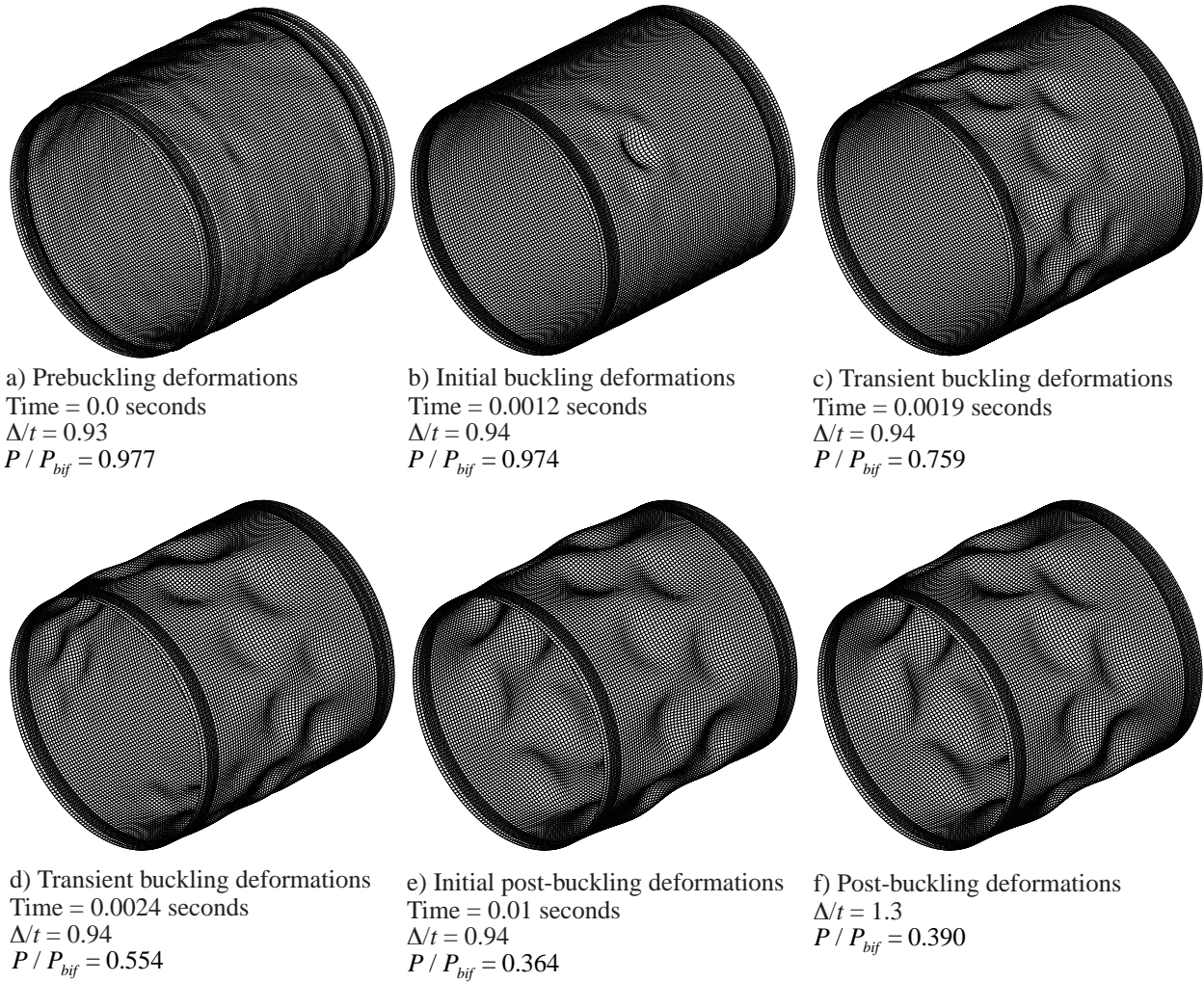
Fig. 7 Numerically predicted prebuckling, buckling, and post-buckling response of an imperfect, compression-loaded, quasi-isotropic shell C3.
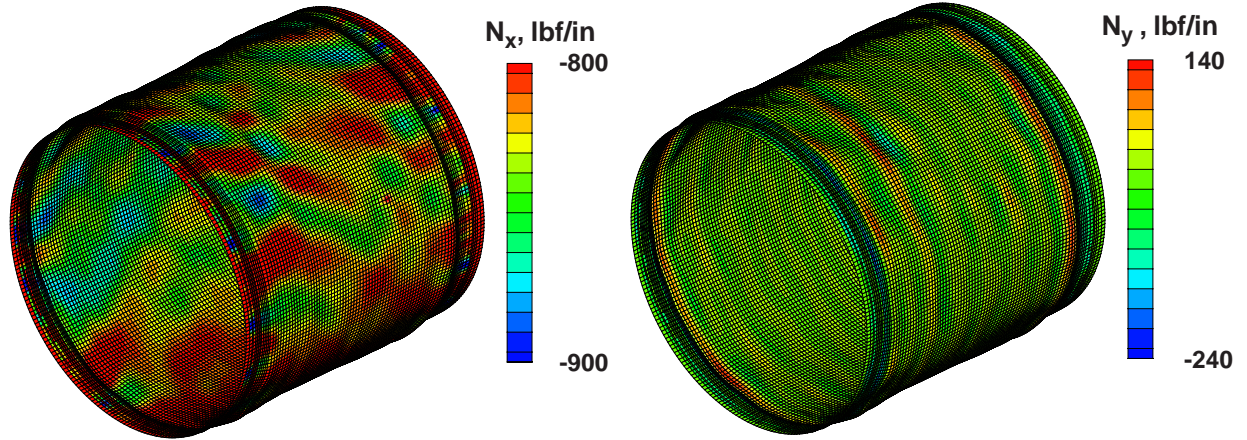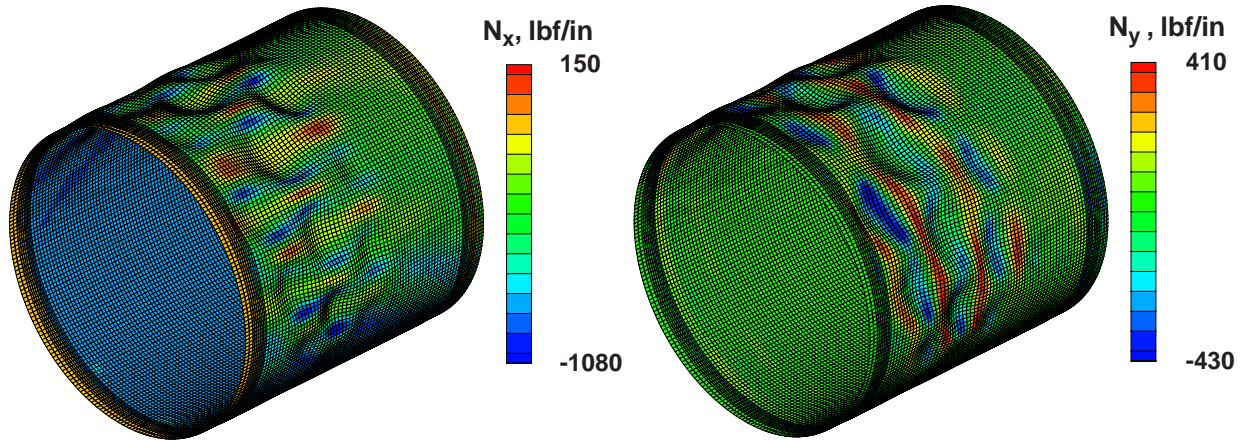
a) Prebuckling stress contours, time = 0.0 seconds, $\Delta/t = 0.93$, $P/P_{bif} = 0.977$

b) Transient buckling stress contours, time = 0.0024 seconds, $\Delta/t = 0.94$, $P/P_{bif} = 0.554$
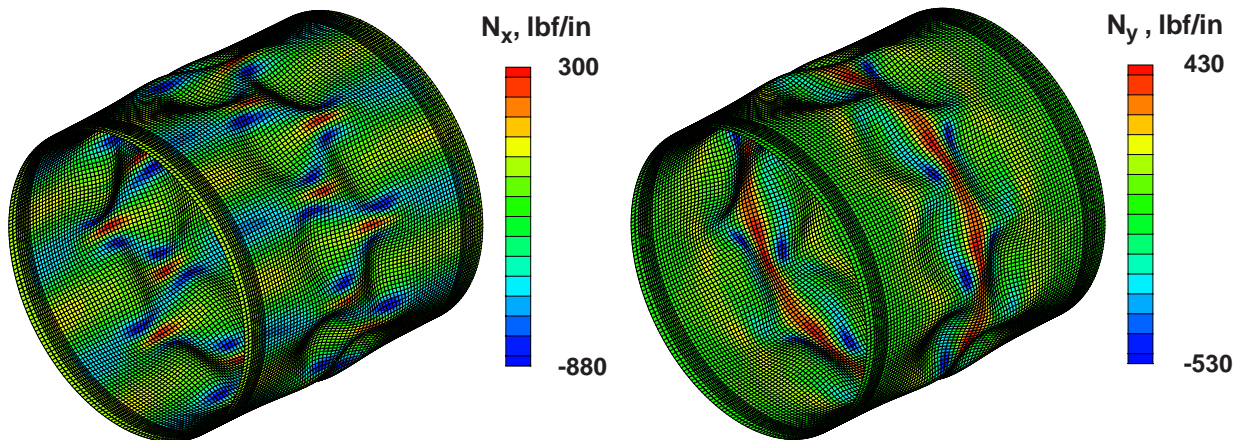
c) Post-buckling stress contours, $\Delta/t = 1.3$, $P/P_{bif} = 0.390$

Fig. 8 Numerically predicted prebuckling, buckling, and post-buckling axial and circumferential stress contours of an imperfect, compression-loaded, 8-ply quasi-isotropic shell C3.
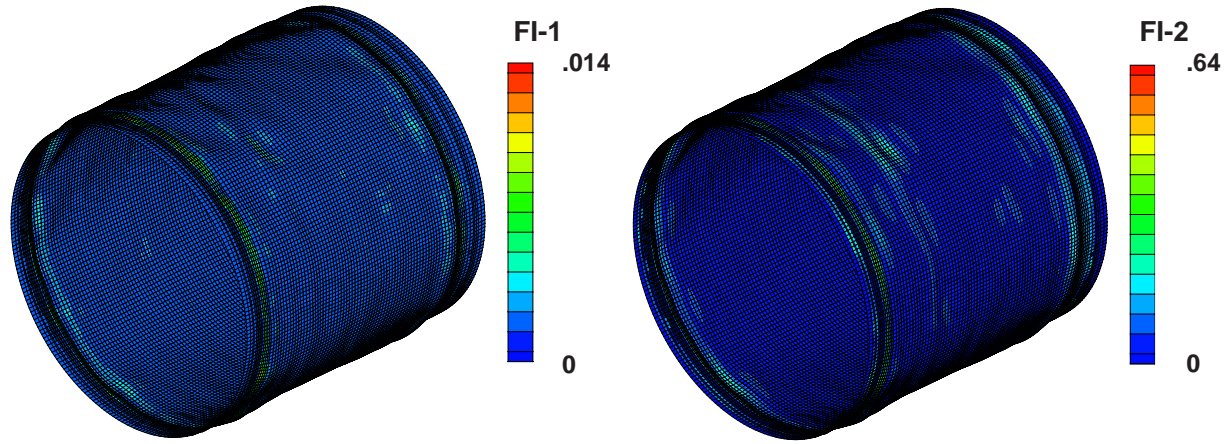
Delamination failures   In-plane fiber or matrix failures

a) Prebuckling failure contours, time $= 0.0$ seconds, $\Delta/t = 0.93$, $P/P_{bif} = 0.977$
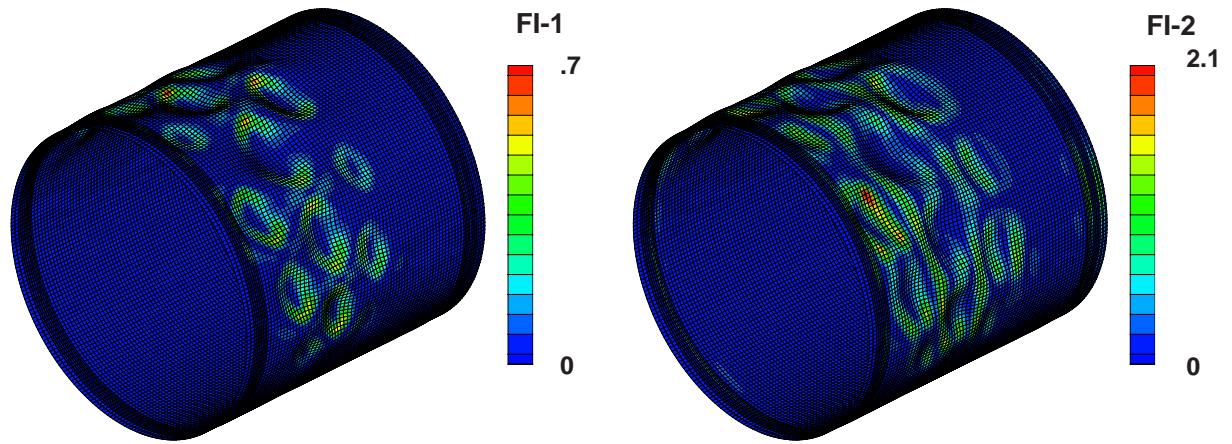
Delamination failures   In-plane fiber or matrix failures

b) Transient buckling failure contours, time $= 0.0024$ seconds, $\Delta/t = 0.94$, $P/P_{bif} = 0.554$
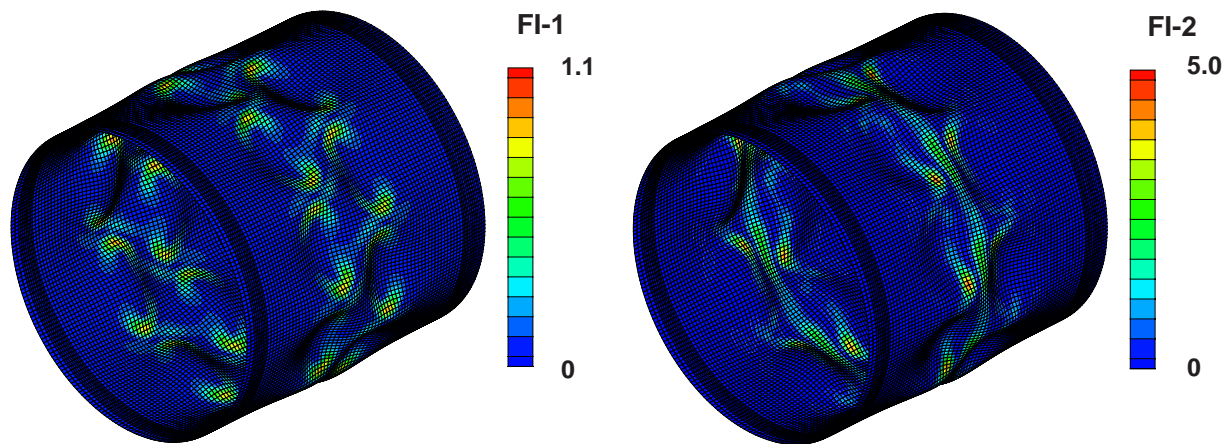
Delamination failures   In-plane fiber or matrix failures

c) Post-buckling failure contours, $\Delta/t = 1.3$, $P/P_{bif} = 0.390$

Fig. 9 Numerically predicted prebuckling, buckling, and post-buckling failure contours of an imperfect, compression-loaded, 8-ply quasi-isotropic shell C3.
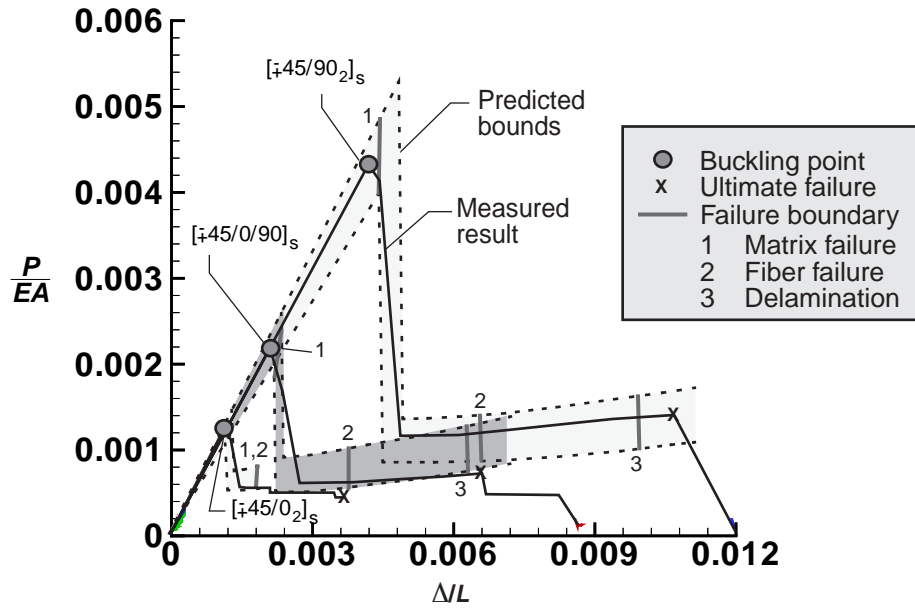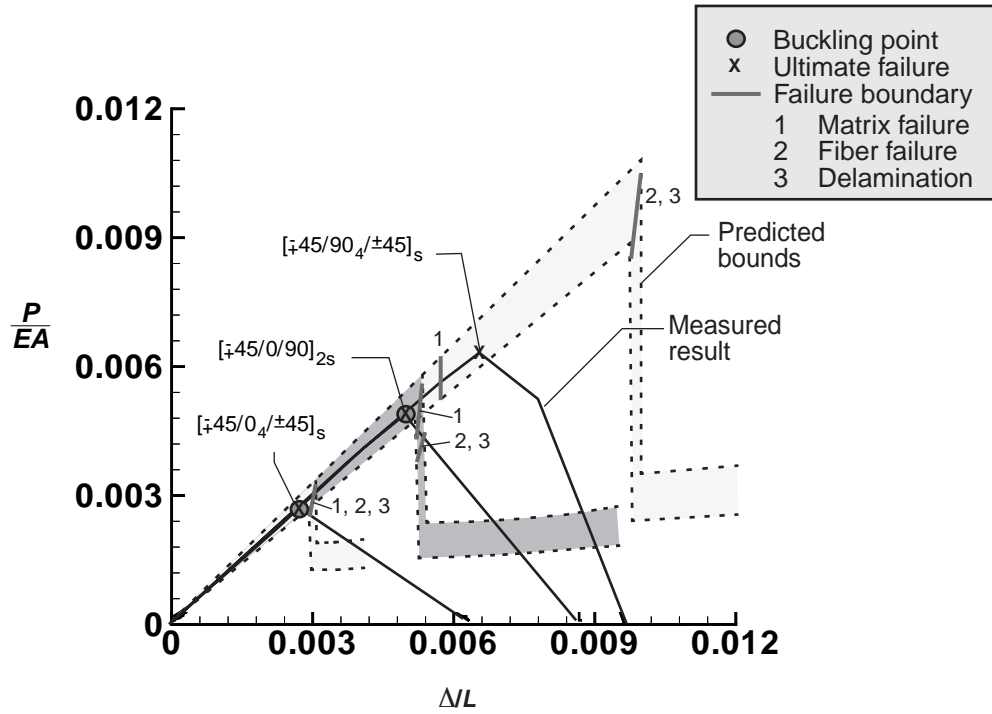
Fig. 10 Numerically predicted and experimentally measured load–end-shortening response curves for 8-ply compression-loaded shells; predicted results represent response bounds.
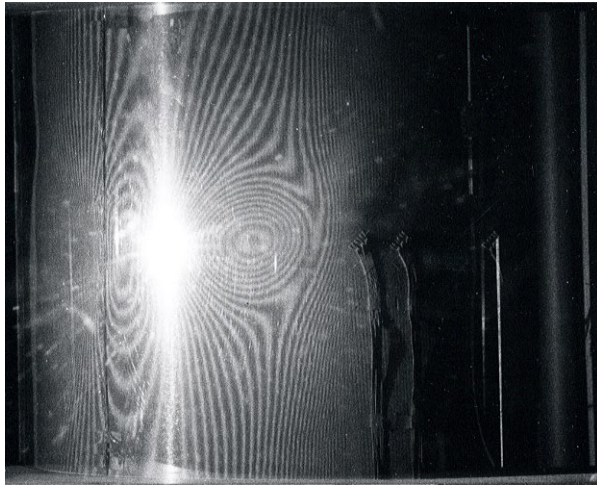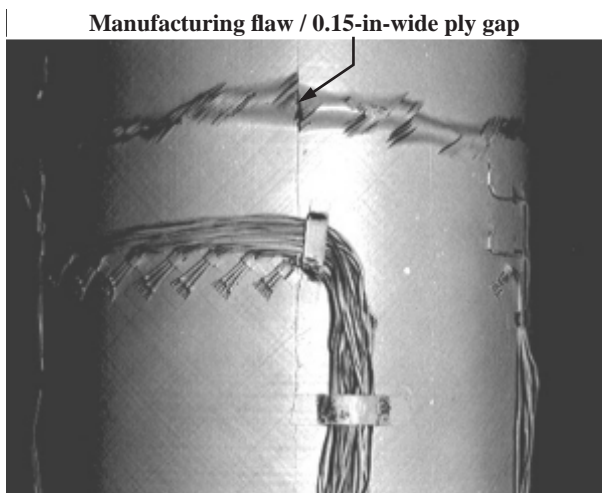

a) Observed post-buckling moiré fringe pattern.
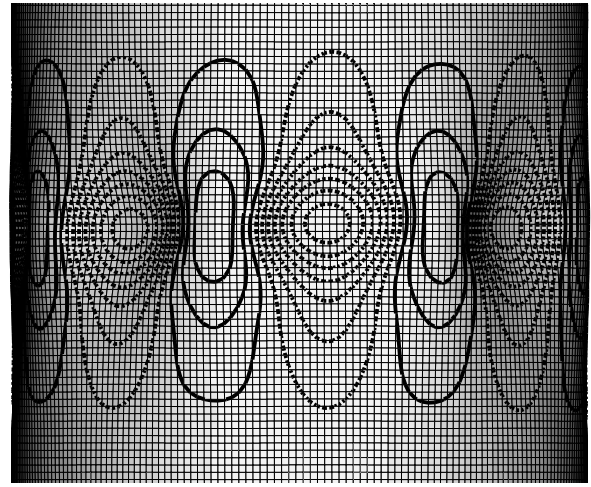
b) Numerically predicted post-buckling normal deformation response.

Fig. 11 Observed and predicted initial post-buckling normal displacements for specimen C1.
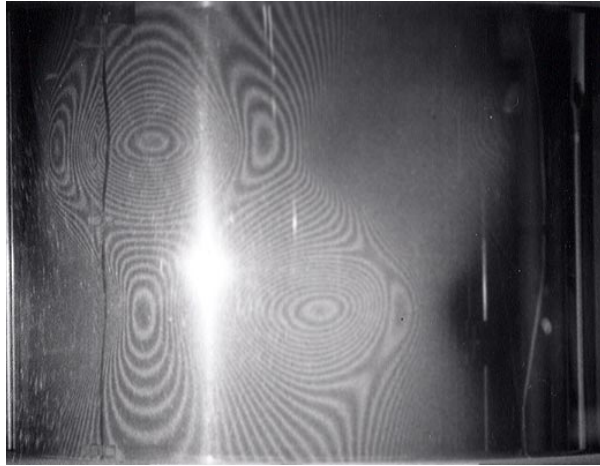
a) Observed post-buckling moiré fringe pattern.
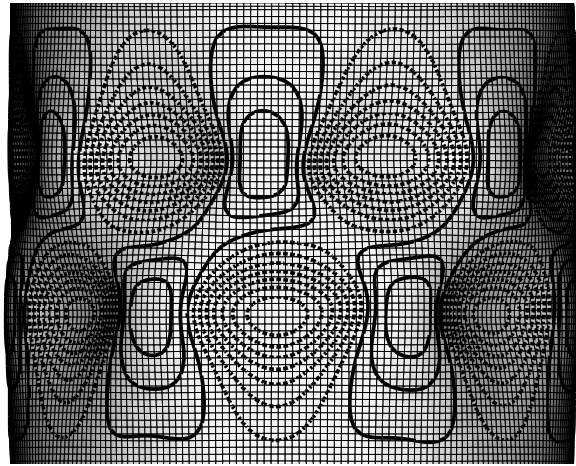
b) Numerically predicted post-buckling normal deformation response.

Fig. 12 Observed and predicted initial post-buckling normal displacements for specimen C2.

Fig. 13 Numerically predicted and experimentally measured load–end-shortening response curves for 16-ply compression-loaded shells; predicted results represent response bounds.
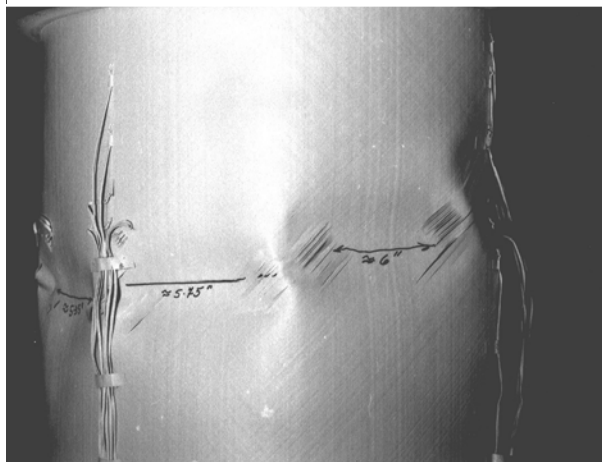
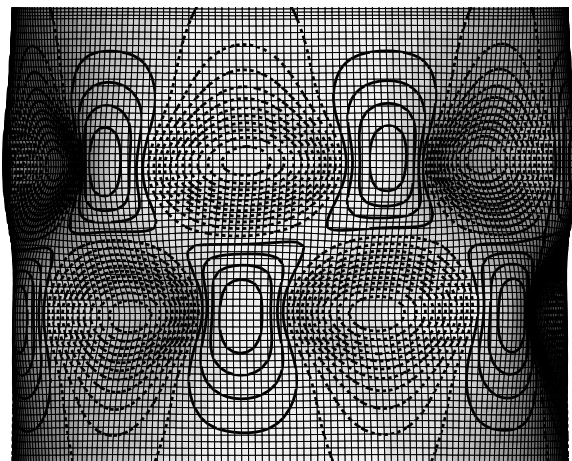a) Observed post-buckling deformation pattern.
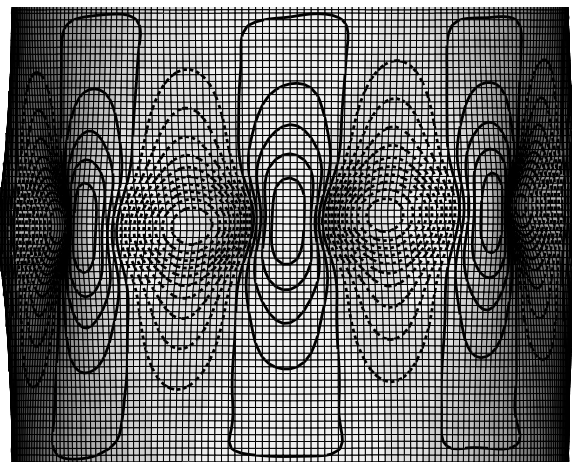
b) Numerically predicted post-buckling normal deformation response.

Fig. 14 Observed and predicted initial post-collapse normal displacements for specimen C5.

Manufacturing flaw / 0.15-in-wide ply gap

a) Observed post-buckling deformation pattern.

b) Numerically predicted post-buckling normal deformation response.

Fig. 15 Observed and predicted initial post-buckling normal displacements for specimen C6.
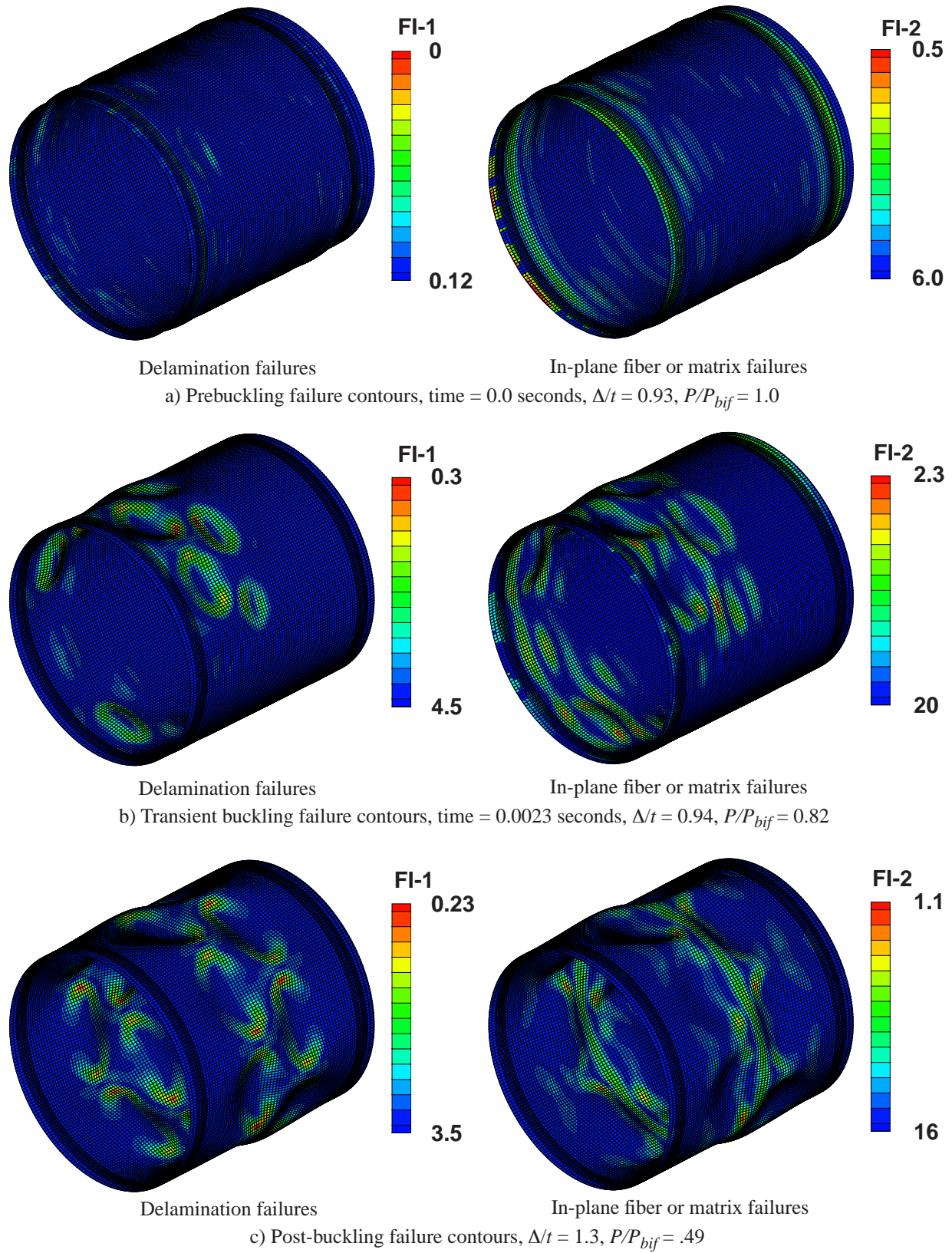
Delamination failures   In-plane fiber or matrix failures

a) Prebuckling failure contours, time = 0.0 seconds, $\Delta/t = 0.93$, $P/P_{bif} = 1.0$

Delamination failures   In-plane fiber or matrix failures

b) Transient buckling failure contours, time = 0.0023 seconds, $\Delta/t = 0.94$, $P/P_{bif} = 0.82$

Delamination failures   In-plane fiber or matrix failures

c) Post-buckling failure contours, $\Delta/t = 1.3$, $P/P_{bif} = .49$

Fig. 16 Numerically predicted prebuckling, buckling, and post-buckling failure contours of an imperfect, compression-loaded, 16-ply quasi-isotropic shell C4.

25

REPORT DOCUMENTATION PAGE

1. REPORT DATE (DD-MM-YYYY)	2. REPORT TYPE	3. DATES COVERED (From - To)
01- 09 - 2004	Tecnical Memorandum	

4. TITLE AND SUBTITLE

Buckling and Failure of Compression-Loaded Composite Cylindrical Shells With Geometric and Material Imperfections

5a. CONTRACT NUMBER

5b. GRANT NUMBER

5c. PROGRAM ELEMENT NUMBER

6. AUTHOR(S)

Hilburger, Mark W.; and Starnes, James H., Jr.

5d. PROJECT NUMBER

5e. TASK NUMBER

5f. WORK UNIT NUMBER

23-719-20-30

7. PERFORMING ORGANIZATION NAME(S) AND ADDRESS(ES)

NASA Langley Research Center
Hampton, VA 23681-2199

8. PERFORMING ORGANIZATION REPORT NUMBER

L-19010

9. SPONSORING/MONITORING AGENCY NAME(S) AND ADDRESS(ES)

National Aeronautics and Space Administration
Washington, DC 20546-0001

10. SPONSOR/MONITOR'S ACRONYM(S)

NASA

11. SPONSOR/MONITOR'S REPORT NUMBER(S)

NASA/TM-2004-212677

12. DISTRIBUTION/AVAILABILITY STATEMENT

Unclassified - Unlimited
Subject Category 39
Availability: NASA CASI (301) 621-0390   Distribution: Standard

13. SUPPLEMENTARY NOTES
An electronic version can be found at http://techreports.larc.nasa.gov/ltrs/ or http://ntrs.nasa.gov

14. ABSTRACT

The results of an experimental and numerical study of the effects of initial imperfections on the buckling response and failure of unstiffened thin-walled compression-loaded graphite-epoxy cylindrical shells are presented. The shells considered in the study have six different orthotropic or quasi-isotropic shell-wall laminates and two different shell-radius-to-thickness ratios. The numerical results include the effects of geometric shell-wall mid-surface imperfections, shell-wall thickness variations, local shell-wall ply-gaps associated with the fabrication process, shell-end geometric imperfections, nonuniform end loads, and the effects of elastic boundary conditions. Selected cylinder parameter uncertainties were also considered. Results that illustrate the effects of imperfections and uncertainties on the nonlinear response characteristics, buckling loads and failure of the shells are presented. In addition, a common failure analysis is used to predict material failures in the shells.

15. SUBJECT TERMS

Shell Buckling; Imperfections, Failure, Composites, Compression load

16. SECURITY CLASSIFICATION OF:			17. LIMITATION OF ABSTRACT	18. NUMBER OF PAGES	19a. NAME OF RESPONSIBLE PERSON
a. REPORT	b. ABSTRACT	c. THIS PAGE			STI Help Desk (email: help@sti.nasa.gov)
U	U	U	UU	30	19b. TELEPHONE NUMBER (Include area code) (301) 621-0390